Investigating intermittent behaviors in transitional flows using a novel time-frequency-based method

Jibin Joy Kolliyil, Nikhil Shirdade, and Melissa C. Brindise

Department of Mechanical Engineering, Pennsylvania State University, University Park, PA, USA

Corresponding Author:

Melissa C. Brindise

Email: mcb5351@psu.edu

Address: 301B Reber Building, University Park, PA, 16802

ABSTRACT

The intermittency characteristics in transitional and turbulent flows can provide critical information on the underlying mechanisms and dynamics. While time-frequency (TF) analysis serves as a valuable tool for assessing intermittency, existing methods suffer from resolution issues and interference artifacts in the TF representation. As a result, no suitable or accepted methods currently exist for assessing intermittency. In this work, we address this gap by presenting a novel TF method—a Fourier-decomposed wavelet-based transform—which yields improved spatial and temporal resolution by leveraging the advantages of both integral transforms and data-driven mode decomposition-based TF methods. Specifically, our method combines a Fourier-windowing component with wavelet-based transforms such as the continuous wavelet transform (CWT) and superlet transform, a super-resolution version of the CWT. Using a peak-detection algorithm, we extract the first, second, and third most dominant instantaneous frequency (IF) components of a signal. We compared the accuracy of our method to traditional TF methods using analytical signals as well as an experimental particle image velocimetry (PIV) dataset capturing transition to turbulence in pulsatile pipe flows. Error analysis with the analytical signals demonstrated our method maintained superior resolution, accuracy and, as a result, specificity of the instantaneous frequencies. Additionally, with the pulsatile flow dataset, we demonstrate that IF components of the fluctuating velocities extracted by our method decompose energy cascade components in the flow. Additional investigations into corresponding spatial frequency structures resulted in detailed observations of the inherent scaling mechanisms of transition in pulsatile flows.

Keywords: Time-frequency analysis, instantaneous frequency, transition to turbulence, intermittency, energy cascade

1. Introduction

Transition to turbulence is characterized by the presence of isolated intermittent turbulent structures known as turbulent puffs (Brindise and Vlachos, 2018; Frishman and Grafke, 2022). This intermittency can induce various deleterious effects across a variety of flow domains, e.g. cardiovascular (Poelma et al., 2015; Trip et al., 2012), nuclear reactor (Yuan et al., 2016; Zhuang et al., 2016), and high-frequency ventilation systems (Einav and Sokolov, 1993). These adverse effects include altering flow behavior (Freidoonimehr et al., 2020; Kefayati and Poepping, 2013; Nerem et al., 1972; Poelma et al., 2015; Sherwin and Blackburn, 2005; Valen-Sendstad et al., 2011), inducing fluctuations in wall shear stress (Peacock et al., 1998), as well as causing rapid increases in friction factor and loss of energy (Yuan et al., 2016). Hence, accurate detection and analysis of transitional flows is of great interest. Unfortunately, limited analysis methods exist that are capable of assessing flows or signals with intermittency, resulting in a critical gap in the current ability to evaluate transitional flows.

At the onset of the transitional regime, localized patches of turbulence are produced in the flow, but are short-lived and rapidly decay. As flow develops through the transitional regime, the turbulent puffs progressively become more frequent and stable to decays (Avila et al., 2011). The localized and intermittent nature of turbulent puffs inherently suggest that they maintain characteristic spatial and time scales. This highlights that time-frequency-based analysis methods can provide the needed framework for evaluating transitional flows. However, while various time-frequency and data mode decomposition methodologies exist for evaluating spectral information,

none provide sufficient temporal and spectral resolution and localization for accurate intermittency analysis.

The Short-Time Fourier Transform and continuous wavelet transform (CWT) are two of the most common TF methods. The Short-Time Fourier Transform temporally windows the signal and takes the Fourier transform of each signal segment. However, the Short-Time Fourier Transform requires a user-inputted window size that induces time and frequency resolution limitations. The CWT mitigates this limitation by incorporating scaling and shifting of a time-localized function, known as the mother wavelet, for improved resolution of the time-frequency representation (TFR). Numerous studies have explored the use of CWT for analyzing flow intermittency (Ruppert-Felsot et al., 2009) and turbulence (Farge, 1992). However, the low frequency resolution at high frequencies inherent to the CWT results in interference artifacts and mode mixing between high-frequency components. Recently, Barzan et al. (2021) and Moca et al. (2021) proposed a CWT-based methodology known as the fractional adaptive superlet transform (FrASLT) to obtain a super-resolution TFR. However, investigating the FrASLT revealed a critical trade-off associated with frequency resolution. Namely, lower frequency resolution TFRs suffered from interference artifacts, while higher frequency resolution TFRs maintained a reduced time resolution, rendering the FrASLT not well suited for analyzing intermittent dynamics.

Data-driven mode decomposition methods provide an alternative approach for TF analysis. These methodologies decompose a signal into its constituent orthogonal components, and the instantaneous frequency (IF) of each component is subsequently calculated. A well-known example of such approach is the empirical mode decomposition—Hilbert-Huang Transform (EMD-HHT) (or simply HHT for brevity) (Huang et al., 1998). The HHT method has been employed to study turbulent flows (Huang et al., 2008). Recently, Singh et al. (2017) proposed

another approach—the Fourier decomposition method—which adaptively decomposes a signal in the Fourier domain. However, both HHT and Fourier decomposition method suffer from mode mixing, especially in the presence of close frequency components, and have been observed to fail for signals with intermittency. Zhou et al. (2022) proposed the empirical Fourier decomposition which decomposes a signal based on the minima in the Fourier domain. However, a major limitation of empirical Fourier decomposition is the requirement of a predefined number of signal components. In general, IFs extracted using decomposition-based methods are prone to erroneous oscillations and in their generic forms are not sufficient for extracting intermittency mechanisms.

In this study, we propose a novel methodology that overcomes the limitations of current time-frequency analysis methods by leveraging the advantages of both integral transforms and data-driven decompositions. Our method is capable of 1) providing an accurate TFR with high spectral and temporal resolution and localization, even in cases where similar frequency components exist in a signal; and 2) extracting multiple dominant IFs within a signal. While our method was designed for use with any type of flow, it is particularly beneficial in the presence of intermittency, which is prevalent in transition flows. Furthermore, it requires no user inputs or a priori knowledge of the signal such that it can be used to extract the frequency components of any arbitrary signal (e.g., hydrophone data to measure pressure fluctuation frequencies, electrocardiogram data to measure fluctuations in the electrical activity of heart, etc.). Our method decomposes a signal into a set of Fourier mode signals and stitches together a single TFR from the wavelet-based transform of each Fourier mode. An adaptive thresholding is used to extract the dominant frequency components efficiently and consistently. We tested and validated our method using analytical signals with known frequency components as well as experimental particle image velocimetry (PIV) data of transitional pulsatile flow from Brindise and Vlachos (2018). To demonstrate the

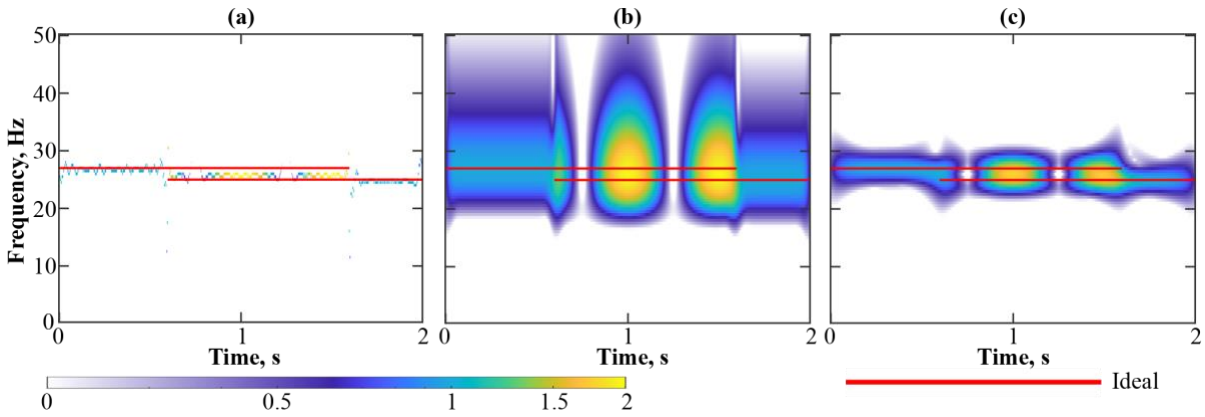

Fig. 1. Time-frequency representation (TFR) computed using (a) HHT (b) CWT (c) FrASLT for an analytical sinusoidal signal with two frequency components: 25 Hz from 0.6-2.0s, 27 Hz from 0-1.6s.

value of extracting the IF components of a flow, we evaluated the coherent nature of the dominant frequency structures in the flow as well as the instantaneous turbulent energy cascade resolved using our approach.

2. Proposed time-frequency analysis method

The intermittency inherent to transitional and turbulent regimes impose that, at any given time instance, multiple structures with varying frequencies are expected to exist within any region of interest. Thus, a TF method suitable for intermittent flow structure analysis must have sufficiently high resolution in both time and frequency such that dominant signal frequency components close in magnitude are separable. Fig. 1 illustrates the observable fringe patterns (i.e., patterned coefficients) in the TFR that occur using (a) HHT, (b) CWT, and (c) FrASLT when multiple near-frequency components exist in a signal (Fig. 1 uses an analytical sinusoidal signal with 25 and 27Hz components from 0.6 s to 2 s and 0 s to 1.6 s, respectively). These interference fringe patterns in turn lead to inaccurate dominant frequency component extraction. Our proposed method mitigates the effect of these interference artifacts by taking advantage of the fact that the Fourier transform provides the highest frequency resolution and can decompose a signal into its mode

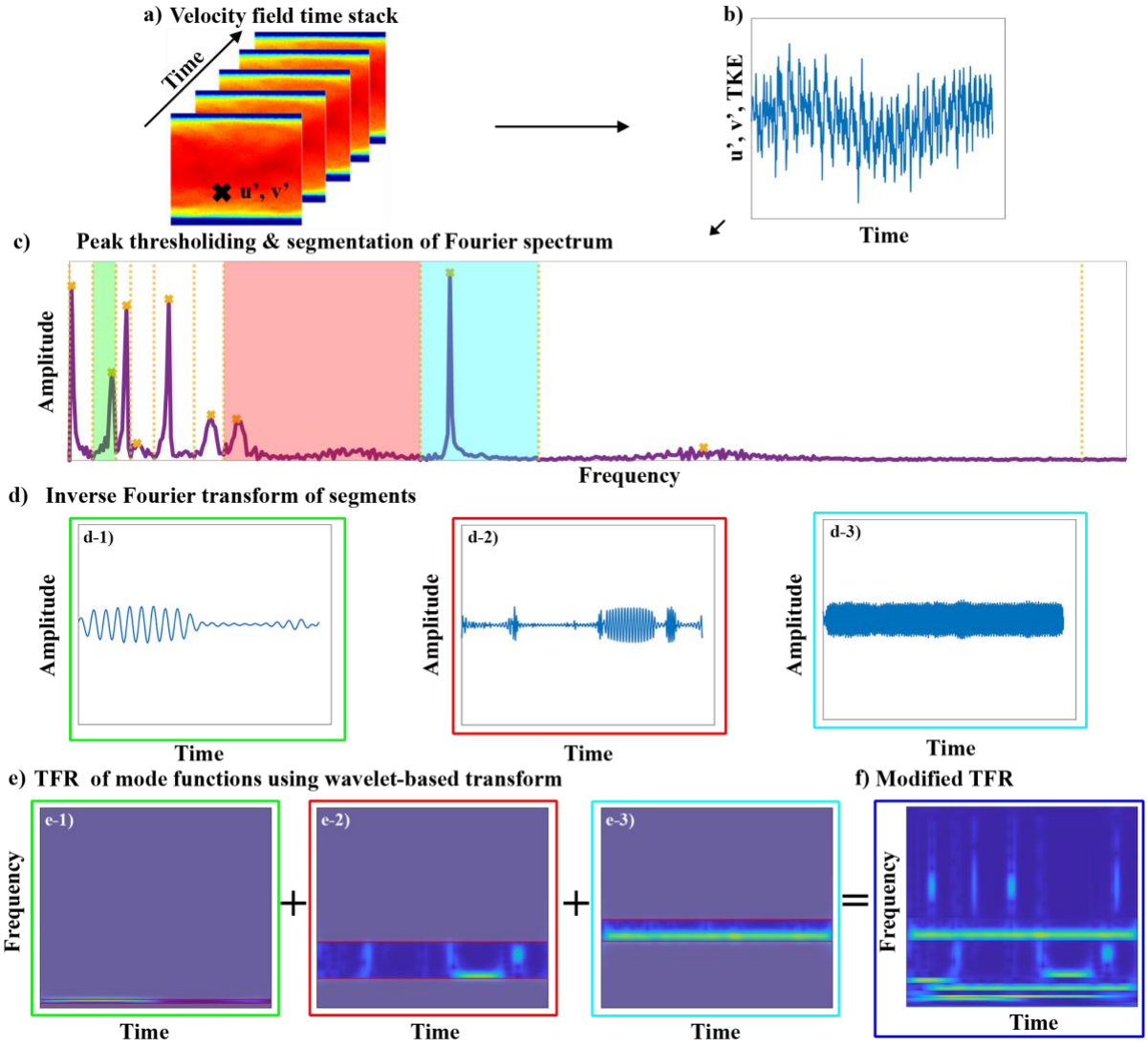

Fig. 1. Proposed time-frequency analysis method. (a) The velocity field time stack. (b) Sample signal representation (shown here as an analytical non-stationary sinusoidal signal with nine frequency components). (c) Extracted peaks and resulting segmentation of Fourier spectrum of the mean-subtracted signal. (d) The real valued mode functions to segments in Fourier spectrum (g) The resulting TFR for each mode functions using wavelet-based transform. (h) The resultant modified TFR after combining TFR corresponding to all mode functions

functions. Hence, combining Fourier-based mode functions with wavelet-based transforms simultaneously removes interference artifacts while maintaining optimal spectral and temporal resolutions. A schematic of our proposed method is provided in Fig. 2 and Fig. 3.

2.1. Decomposing the input signal into Fourier modes

While the input signal (Fig. 2b) could be any arbitrary signal, for our purposes herein where intermittent flow analysis is of interest, the fluctuating velocity or turbulent kinetic energy (TKE)

should be inputted. (We note that Fig. 2b shows the analytical non-stationary signal defined by summing nine independent sinusoidal components that we use to demonstrate our method.) The input signal is mean-subtracted, and its Fourier spectrum is subsequently calculated using the standard fast Fourier transform (FFT) (Fig. 2c). All peaks of the Fourier spectrum are identified using the built-in *findpeaks* function in MATLAB. This function identifies local peaks in a signal, returning the magnitude, location, width, and prominence of each identified peaks. Noisy peaks—which are expected to exist due to the non-stationary nature of the input signal—are filtered out using a peak prominence thresholding. Specifically, a histogram of the peak prominence of all peaks is computed based on the built-in *histcounts* function in MATLAB, which partitions the input data into a histogram using an automated uniform binning. The resulting peak prominence threshold (τ) is obtained by (Yochum et al., 2016),

$$\tau = \frac{\sum_{i=1}^{nb} c_i \times N_i}{\sum_{i=1}^{nb} N_i} \quad (1)$$

where c_i represent the peak prominence value corresponding to center of each histogram bin, N_i represent the number of peaks corresponding to each histogram bin and nb represent the total number of histogram bins. All peaks with a prominence less than this threshold value are considered as noisy and removed. The Fourier spectrum with the final, filtered peaks identified is shown in Fig. 2c. The FFT is then windowed where the edges of each window are defined as the frequency corresponding to the minimum FT magnitude between adjacent frequency peaks (Fig. 2c). The Fourier spectrum slices for the first and last peak are closed using the respective negative and positive Nyquist frequency. Hence, this represents an adaptive windowing scheme where the entire spectrum is segmented such that prominent frequency components are expected to exist within each spectral slice. Next, an ideal band pass filter was applied to each positive spectral slice to generate time-domain representation of the mode function corresponding to each window and

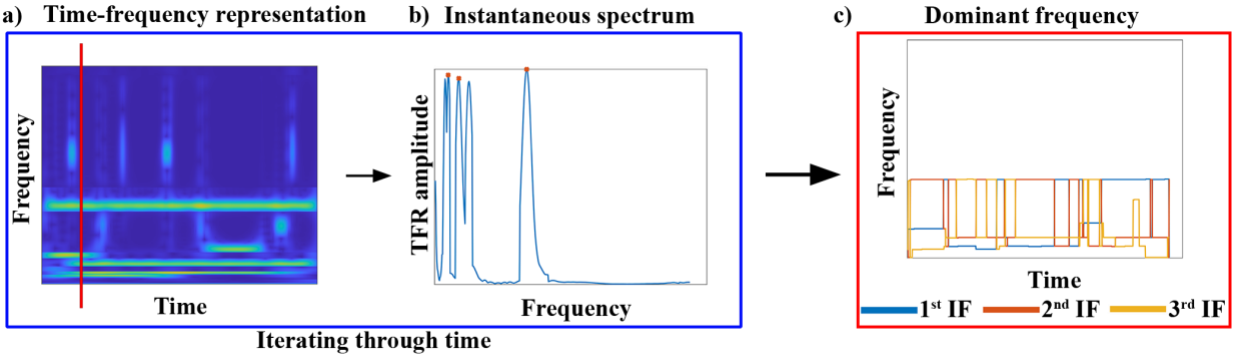

Fig. 2. Extraction of instantaneous dominant frequency packet. (a) The modified TFR using Fourier decomposition (b) Instantaneous spectrum at specific time instant (c) Extracted dominant frequencies after iterating through time

the Hilbert transform was used to obtain the analytical representation of the mode functions as shown in Fig. 2d. As evident from Fig. 2d-1 and 2d-2, the mode functions exhibit similar forms of nonstationary behavior as the original signal and contain notably different frequency magnitudes.

2.2. Calculating the time-frequency representation

A CWT-based transform is used to calculate the TFR of each Fourier mode. We employed the FrASLT method since it provides an adaptive resolution in frequency as compared to the general CWT. However, the CWT can also be used and herein we test both approaches. Fig. 2e shows the TFR coefficient maps computed using the FrASLT for each Fourier mode from Fig. 2d. All TFR coefficients outside of the corresponding frequency window of each Fourier mode are set to zero. A single TFR coefficient map (Fig. 2f) for the input signal is generated by summing together the TFR coefficient maps of all Fourier mode signals.

2.3. Extracting the instantaneous dominant frequency packet

Using the final TFR coefficient map (Fig. 3a), the dominant IFs are extracted through an iterative process. Specifically, the peaks of each column of the resultant TFR coefficient map (i.e., each individual time point) are identified using the built-in *findpeaks* function in MATLAB (Fig. 3a and 3b). To close the 1-D TFR coefficient columns prior to peak finding, the TFR coefficient values at the boundaries (i.e., 0Hz and the Nyquist frequency) needed to be set manually. This closure of

the TFR at the boundaries was done to extend the signal, so that any endpoint peaks could be identified in the same manner as other peaks, i.e. using the prominence-based peak identification and analysis. For 0Hz, the mean value of the input signal was used, while a symmetric behavior of the TFR was assumed around the Nyquist frequency. The extracted peaks were sorted according to their peak prominence. The frequency and TFR coefficient of the peaks with highest prominence were identified. Finally, the resultant peaks were further sorted based on the TFR coefficients to determine dominance levels. Fig. 3c illustrates the extracted 1st, 2nd, and 3rd IFs of the input signal. In its current form, our method extracts at most three dominant frequencies for a given time step. However, our method can be readily expanded to extract additional frequency components, a notion that will be explored in future work.

We termed our method as the Fourier-Decomposed Superlet Transform, or FDST, method. For the implementation where the CWT was used in place of the FrASLT, we refer this as the Fourier-Decomposed CWT, or FDCWT, method.

3. Implementation details for comparison methods (HHT, CWT, FrASLT)

The complex Morlet wavelet with a standard deviation value of five for the Gaussian envelop was considered for all wavelet-based calculations. Since the time domain-based CWT calculation resulted in major artifacts near scales corresponding to the Nyquist frequency, the frequency domain-based CWT calculation was implemented. The resulting L1 norm CWT calculation (Addison, 2017; Lilly, 2017) is given by,

$$T_x(a,b) = \int_{-\infty}^{\infty} X(f)\Psi^*(af)e^{i2\pi fb}df \quad (2)$$

where T represents the CWT coefficients, x represents the input signal, X represents the Fourier transform of input signal, Ψ represents the Fourier transform of mother wavelet, a represents the scale parameter, and b represents the shift parameter. The CWT was numerically implemented using the FFT algorithm with appropriate zero padding in order to reduce wrap-around artifacts.

For both the FrASLT and FDST, an initial cycle of three and order of 20 was chosen. Through testing, these values were found to optimally minimize computational time while reducing the loss of information. For consistency, the cycle parameter of the complex Morlet wavelet was also chosen as three for both the CWT and FDCWT calculations. The built-in MATLAB functions of *emd* and *hht* were utilized for extracting the mode functions and Hilbert spectrum of the HHT calculations.

4. Analytical Signal Analysis

4.1. Analytical test signals set

4.1.1. Data generation

Two sets of non-stationary sinusoidal test signals with two frequency components were created. To match typical experimental data resolution, a sampling frequency of 250 Hz and signal length of 500 datapoints were used, resulting in signals of 2 second (s) length.

The first set of test signals contained frequency components with constant amplitude which are turned on and off at specific time instants. The first frequency component existed in the signal from 0.6s to 2s with an amplitude of 1.1 (referred to here as the major component or major frequency (F_m)), while the second frequency component existed from 0s to 1.6s with an amplitude of 1 (referred to here as the minor component or minor frequency (F_n)). A set of signals were generated where the major frequency was fixed as 50Hz and the minor frequency was varied across

signals with values of 10Hz, 46Hz, and 90Hz. Additional test signals were generated where both the major and minor frequencies varied from 0.5Hz to 125Hz (the Nyquist frequency).

The second set of test signals contained frequency components with varying amplitudes as well as added noise. The frequency of the first component was fixed at 50Hz. Its amplitude varied linearly from 0 to 1 between 0s and 0.6s, and from 1 to 0 between 0.6s and 2s. The frequency of the second component was fixed at 46Hz and its amplitude varied linearly from 0 to 1 between 0s and 1.6s, and from 1 to 0 between 1.6s and 2s. The incorporation of ramped-on and ramped-off amplitude was expected to imitate the realistic behavior of turbulent intermittency. Zero-mean uniform white noise was added at noise percentages (defined as the ratio between the standard deviation of the white noise and that of the noiseless signal) of 10%, 100%, and 500%. A total of 1000 instances of the signal set were created using the Mersenne Twister generator, with seed ranging from 1 to 1000 for each instance.

4.1.2. Post-processing calculations

Error analysis of the extracted IFs was conducted for all cases of analytical signals. For the constant amplitude test signal set, the major and minor frequencies of each signal were considered the ground-truth 1st and 2nd IFs, respectively. Since both frequency components were only present from 0.6s to 1.6s, error analysis was limited to this region. The root mean square error (RMSE) metric was used to quantify error between the extracted and true IFs. The RMSE calculations is given by:

$$RMSE = \sqrt{\frac{\sum_{t=0.6}^{t=1.6}\left(IF_e(t) - IF_g(t)\right)^2}{N_{overlap}}} \tag{3}$$

where IF_e and IF_g represent the extracted and ground truth IFs in the region with two frequency components while $N_{overlap}$ represents the number of time points with two frequencies present.

Any missing values in the extracted IFs was assumed to have an error equivalent to the Nyquist frequency as a penalty. Here, missing values in the extracted IFs refers to the case where a ground-truth frequency existed but no corresponding IF was identified by the TF analysis method.

For the varying amplitude test signal set, the ground truth 1st and 2nd IFs were determined as the frequency with the larger amplitude and smaller amplitude, respectively, at a given time instant. At 0s and 2s, where the amplitude of both components were zero, the ground truth for the 1st IF was assumed as the frequency which had higher amplitude immediately at the immediately adjacent time instant. The RMSE calculation was performed over full time length for these signals.

4.2. Method comparison using analytical signals

4.2.1. Constant amplitude test signals

We first compared our methods (FDST and FDCWT) against the current state-of-the-art methods (HHT, CWT, FrASLT) using the set of analytical signals with constant-amplitude ground-truth IFs. Fig. 4 shows the TFRs from (a) HHT, (b) CWT, (c) FrASLT, (d) FDCWT, and (e) FDST. Each row represents a different analytical signal with a major frequency of 50 Hz and a minor frequency of (-1) 10 Hz, (-2) 46 Hz, and (-3) 90 Hz. The red lines denote the ground-truth frequency. Fig. 4 demonstrates the low frequency resolution inherent to the CWT at higher frequencies. Specifically, in Fig. 4b-1, the 50 Hz frequency is represented by a wide band in the coefficient map, whereas the 10 Hz frequency maintains a considerably thinner frequency band. The FrASLT—a super resolution wavelet transform—mitigates this variable frequency resolution by combining multiple wavelet transforms with increasing timescale resulting in high frequency resolution at high frequencies. The FDST method similarly maintained super resolution in frequency at high frequencies, while the FDCWT still exhibited the wide bands caused by the inherent variable frequency resolution issues of the CWT. Fig. 4 also demonstrates that

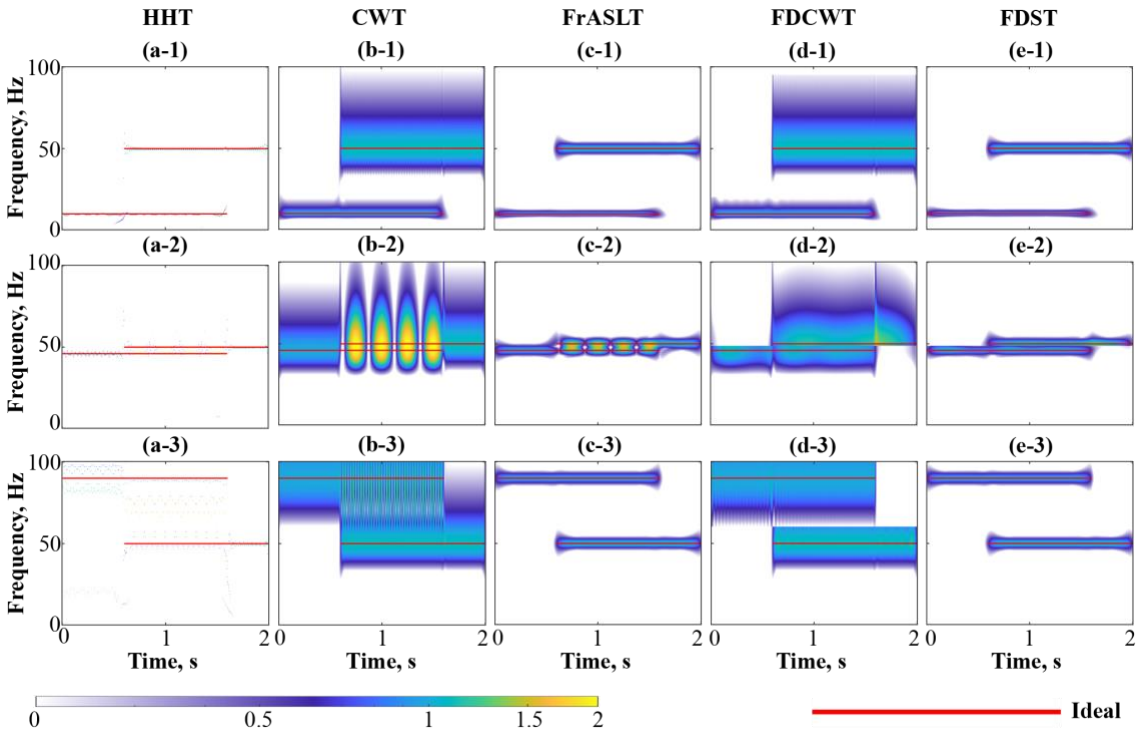

Fig. 4. Extracted TFR of the analytical signal with major components of 50Hz and minor component of (1) 10 Hz, (2) 46 Hz, (3) 90 Hz, using the (a) HHT (b) CWT (c) FrASLT (d) FDCWT and (e) FDST.

insufficient frequency resolution causes mode mixing. Mode mixing is exhibited by a distinct intermittent 'dotted' pattern in the coefficient field. Mode mixing is particularly observed in Fig. 4b-2 and Fig. 4c-2, the case where the major and minor frequency components maintain only a 4Hz difference. Overall, mode mixing was observed for the HHT, CWT, and FrASLT methods. Using our proposed FDST or FDCWT methods, no intermittent patterns are present. This shows the efficacy of our Fourier mode decomposition algorithm component at sufficiently addressing mode mixing by segmenting even close frequency components into individual modes.

Fig. 5 shows the extracted 1st and 2nd IFs of the set of analytical signals from Fig. 4 using each method. The IFs extracted by HHT had significant inaccurate oscillations, especially at higher frequencies. For instance, for the case with a minor frequency of 46Hz (Fig. 5a-3), the extracted 1st IF in the mono-frequency time-frame of 0 to 0.6s oscillated within the range of 44 to 48Hz. For the case with a high minor frequency of 90Hz (Fig. 5a-5), a larger oscillation range of 80 to 98Hz

was observed for this mono-frequency time-frame. When two frequency components were present from 0.6s to 1.6s, the 1st HHT IF showed significant oscillations within the range of 44 to 81Hz (Fig. 5a-3), and 46 to 89Hz (Fig. 5a-5) for cases with minor frequencies of 46 Hz and 90 Hz, respectively. Such behaviors in the extracted frequencies using HHT can be attributed to the anomalous extraction of IMFs near the Nyquist frequency. Oscillations in the CWT-extracted 1st IFs varied from 48 to 60Hz (Fig. 5b-3) and 49 to 87Hz (Fig. 5b-5) for the signals with minor frequencies of 46Hz and 90Hz, respectively. For the CWT, the number of oscillatory peaks in the

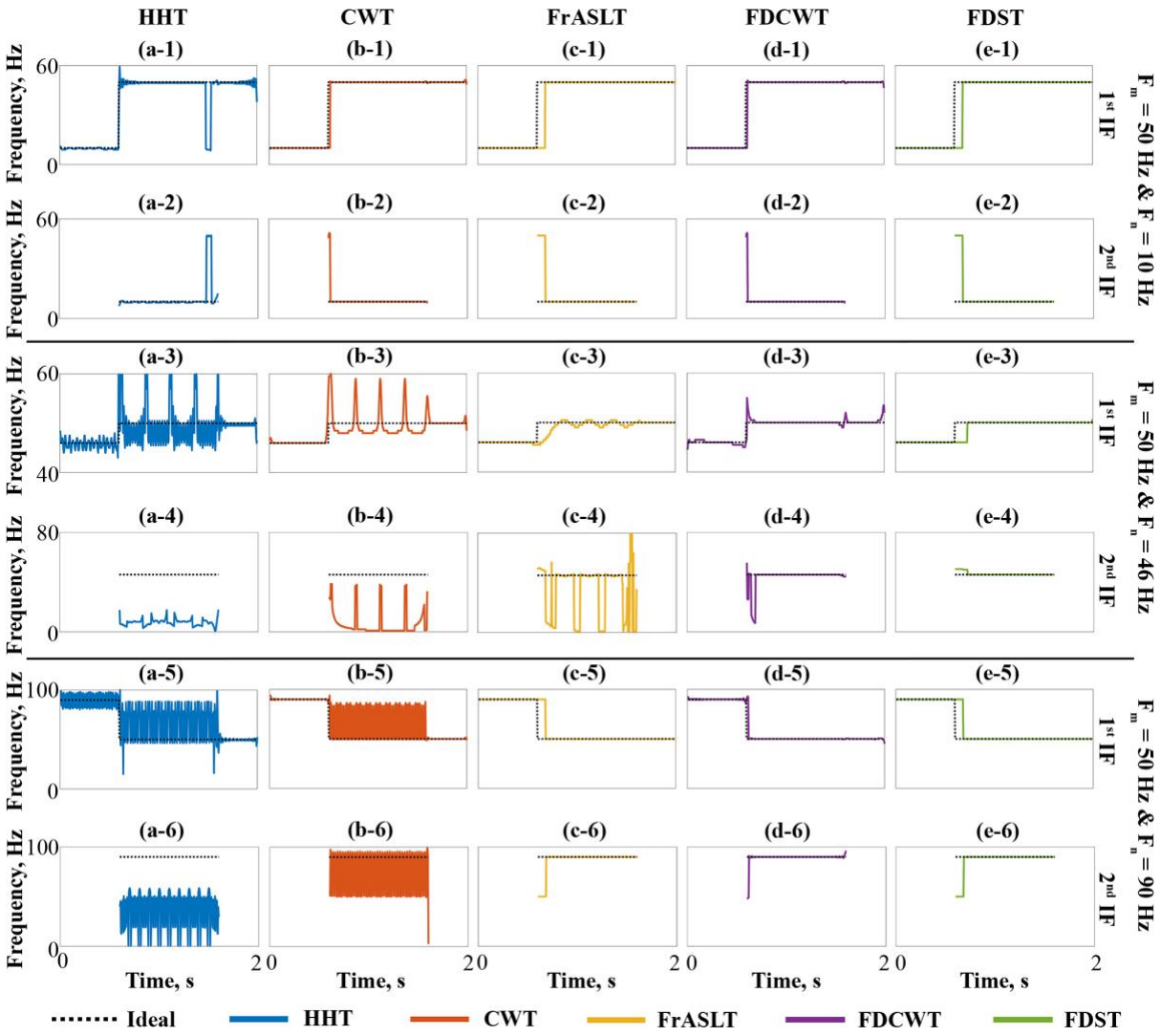

Fig. 5. The extracted both 1st and 2nd IF of the analytical signal with major frequency component (F_m) of 50 Hz and minor frequency component (F_n) of 10 Hz, 46 Hz and 90Hz using (a) HHT, (b) CWT, (c) FrASLT, (d) FDCWT and (e) FDST.

extracted frequencies were observed to correlate with the number of intermittent dotted patterns in the TFR (as evident from Fig. 5b-3 and Fig. 4b-2), implying an association with mode mixing. The super-frequency resolution of the FrASLT method eliminated these oscillations at high frequencies (e.g., Fig. 5c-5 and 5c-6). However, for the signal with close frequency components (Fig. 5c-3 and Fig. 5c-4) oscillatory behavior was still observed, highlighting that limitations in the super-resolution frequency persist. Moreover, the improved frequency resolution is observed to come at the cost of reduced time resolution, resulting in the delayed detection of the dominant frequency change at 0.6s, as observed in all cases of Fig. 5c. IFs extracted using FrASLT identified the change of dominant frequency at 0.68s, a 13% deviation from the ground truth. Both implementations of our proposed method extracted IFs with significant reductions in oscillatory behavior, implying an improved frequency resolution. The frequencies extracted using FDST exhibited the lowest degree of oscillatory behavior while the only oscillatory behavior exhibited by FDCWT occurred at the

Table 1. The RMSE (in Hz) of 1st and 2nd IF extraction with ground truth using HHT, CWT, FrASLT, FDCWT and FDST

Method / Freq.	HHT	CWT	FrASLT	FDCWT	FDST
1st IF					
10 & 50 Hz	9.44	5.65	11.57	5.05	11.57
46 & 50 Hz	6.15	3.11	1.46	0.63	1.43
90 & 50 Hz	23.11	22.89	11.57	5.93	11.57
2nd IF					
10 & 50 Hz	9.07	5.75	11.57	5.15	11.57
46 & 50 Hz	38.45	41.52	26.08	7.69	1.55
90 & 50 Hz	54.64	28.79	11.57	5.90	11.57

0.6s and 1.6s time instances, corresponding to start and end of the minor frequency component. Furthermore, the improved frequency resolution resulted in accurate 2nd IF extraction, suggesting that both implementations of the proposed method were better than the other methods at identifying the primary and secondary signal mechanisms at high frequencies, which is particularly important when analyzing intermittency. However, the FDST method could not resolve the inherent time-resolution limitation of the FrASLT. FDST identified the dominant frequency change (which truly occurred at 0.6s) at 0.68s, 0.72s, and 0.68s in cases with minor frequencies of 10Hz, 46Hz and 90Hz, respectively.

To quantitatively summarize these notions, Table 1 provides the RMSE values, comparing the extracted frequencies vs. the ground-truth frequencies for each method across the analytical signals. The IFs extracted using HHT generally maintained the highest average RMSE across all three signals of 12.90Hz and 34.05Hz for the 1st and 2nd IFs, respectively. With CWT, the mode mixing precipitated a fourfold and fivefold increase in the RMSE of the 1st and 2nd IF, respectively, when the minor frequency increased from 10Hz to 90Hz. At signals with higher frequencies, the super resolution of the FrASLT method yielded a 49% RMSE improvement in the 1st IF as compared to CWT. However, the delayed frequency changepoint detection induced a 51% RMSE increase for the 1st IF with FrASLT as compared to CWT. For FDCWT, an RMSE improvement of 11%, 80%, and 74% was observed in the 1st IF extraction as compared to CWT for signals with minor frequency of 10Hz, 46 Hz, and 90 Hz, respectively. Similarly, for the 2nd IF, an RMSE improvement of 10%, 81%, and 80% for the 10Hz, 46Hz, and 90Hz signals, respectively, was observed. For the 46Hz minor frequency signal, FDST provided a 2% and 94% RMSE improvement over FrASLT for the 1st and 2nd IF extraction, respectively. No significant RMSE

differences were observed between FDST and FrASLT for the analytical signals with well separated frequency components.

Fig. 6a and 6b extend the analysis by showing the RMSE for the 1st and 2nd IF extractions, respectively, as a function of all major and minor frequency combinations (from 0.5Hz to the Nyquist frequency). The global mean RMSE of the 1st IF for all frequency ranges were 26.85Hz, 14.72Hz, 13.40Hz, 8.56Hz, and 13.66Hz for HHT, CWT, FrASLT, FDCWT, and FDST, respectively. Fig. 6a-1 and 6a-2 demonstrate the noted anomalous behavior of the IMFs for HHT and mode mixing for CWT were pervasive problems across the major and minor frequency combinations. High RMSE regions were not observed with FrASLT, FDCWT, and FDST implying a sufficient time-frequency resolution for all frequency ranges. Fig. 6c provides the mean RMSE value as a function of major frequency. At major frequencies below 20Hz, both FDCWT and CWT performed comparably, owing to the high frequency resolution of CWT at low frequencies. However, as frequency increased above 20Hz, a significant increase in the mean RMSE of CWT is observed suggesting 20Hz as the threshold above which mode mixing becomes significant for the CWT method. However, both FDST and FrASLT performed inferiorly compared to CWT at frequencies below 40Hz. This highlights that below 40 Hz, the reduced time resolution of the FrASLT method is more consequential than the advantage of the increased frequency resolution. It is important to note that the thresholds described in this analysis are specific to the characteristics of the chosen signal and analysis parameters; for other signals or analysis parameters, these threshold values should be re-evaluated. FDCWT maintained a 42% improvement of global mean RMSE over CWT, as well as a 36% improvement over FrASLT, and a 37% improvement over FDST. The superior performance of the FDCWT method demonstrates it advantageously leverages the benefits of both the Fourier decomposition step and CWT time-

resolution. The slight reduction in performance of FDST compared to FrASLT in terms of RMSE occurred due to inconsistencies near the Nyquist frequency. Fig. 6d shows the average RMSE of the 2nd IF extraction as a function of the major frequency. A global mean RMSE of 41.64Hz, 38.82Hz, 17.55Hz, 13.94Hz, and 15.06Hz were observed for the HHT, CWT, FrASLT, FDCWT, and FDST respectively. FDCWT and FDST provided a 64% and 14% improvement in the overall RMSE of the 2nd IF as compared to the respective baseline cases (CWT and FrASLT, respectively). This further reiterates that the 2nd IF extraction was greatly influenced by the frequency resolution. FDST was found to perform better for the 2nd IF as compared to FDCWT at higher frequencies

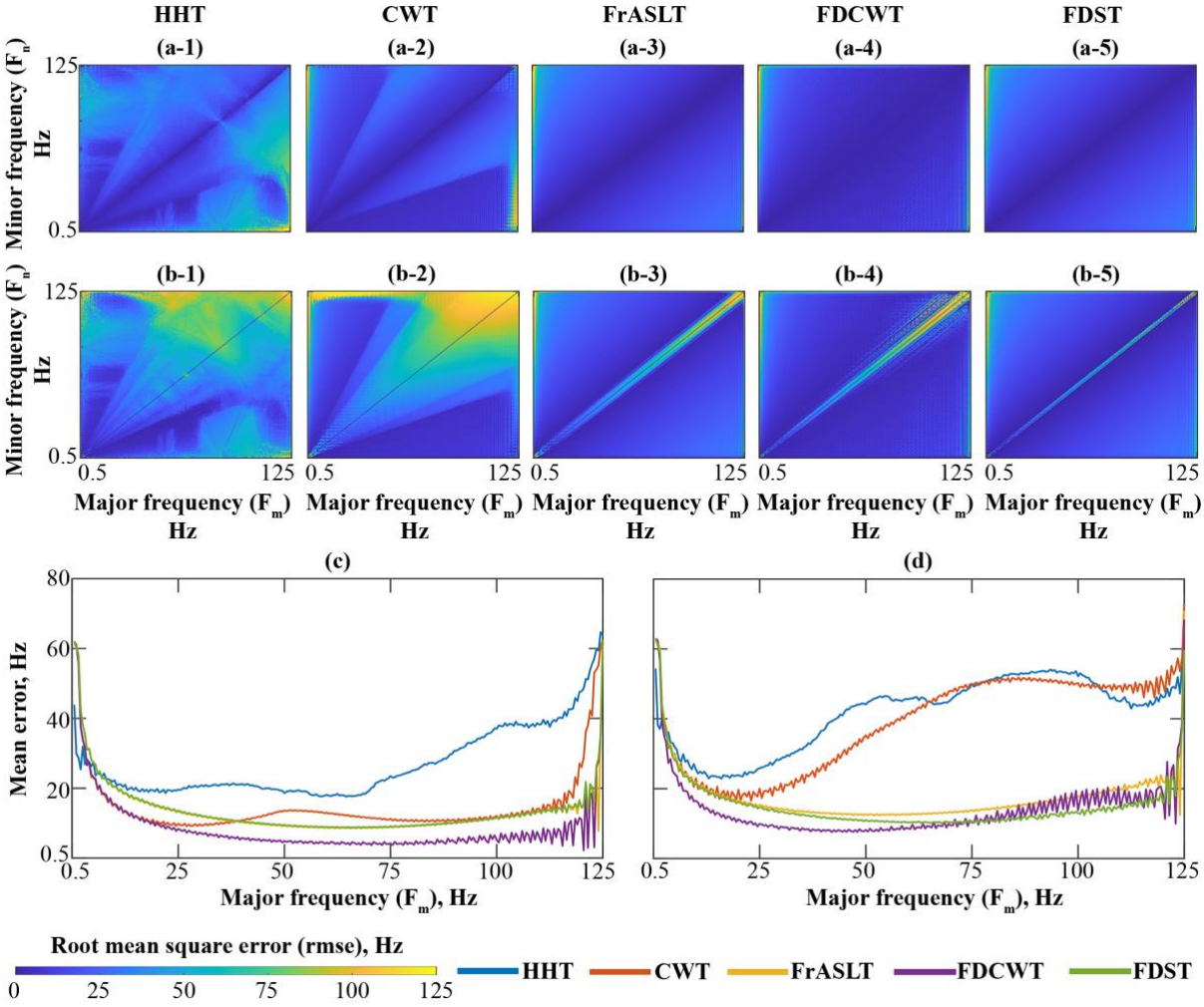

Fig. 6. RMSE as function of major and minor frequencies for (a) 1st and (b) 2nd instantaneous frequencies using the (1) HHT (2) CWT (3) FrASLT (4) FDCWT and (5) FDST. The mean RMSE as function of major frequencies for (c) 1st and (b) 2nd instantaneous frequencies.

implying the suitability of FDST in the extraction of high frequency secondary dynamics. In general, the superiority of FDCWT and FDST points to the importance of the Fourier decomposition step when extracting the underlying secondary dynamics.

4.2.2. Varying amplitude test signals

Next, we evaluate the efficacy of our methods against current state of art methods, for signals with varying frequency amplitudes and added noise. Fig. 7. illustrates the three raw signals used for testing and the extracted 1st and 2nd IFs using each method. With added noise, HHT maintained large oscillations in the 1st IF, while at 100% and 500% noise the ground truth frequency trend was no longer observable. CWT identified the 1st IF accurately, with oscillations ranging from 38Hz to 55Hz for 10% noise (Fig. 7b-1) and 20Hz to 100Hz (Fig. 7b-3) for 100% noise. By 500% noise, the ground truth frequency trend was lost (Fig. 7b-5). For all noise percentages, both HHT and CWT failed to identify the 2nd IF. FrASLT identified the 1st IF with oscillations of amplitude 1Hz for 10% noise, 6Hz for the 100% noise, and up to 70Hz for 500% noise. FDCWT exhibited similar performance to FrASLT, with two main differences of: 1) for 100% noise, low amplitude (48 – 54 Hz range) oscillations when the higher frequency component was dominant (Fig. 7d-3) and 2) slightly less oscillations at 500% noise. The FDST maintained the lowest oscillatory behavior in the 1st IF of all methods, exhibiting some large oscillations at the beginning and end of the signal. For FrASLT, FDCWT, and FDST, in the 500% noise case, a delay in the detection of the dominant frequency changepoint of about 18% was observed in the 1st IF. Both FrASLT and FDCWT largely failed to identify the 2nd IF. FDST successfully identified the 2nd IF with minimal oscillations for the 10% case. For the 100% noise case, 2nd IF oscillations at the beginning and end of the signal were observed, while for the 500% noise case, the 2nd IF was not resolved.

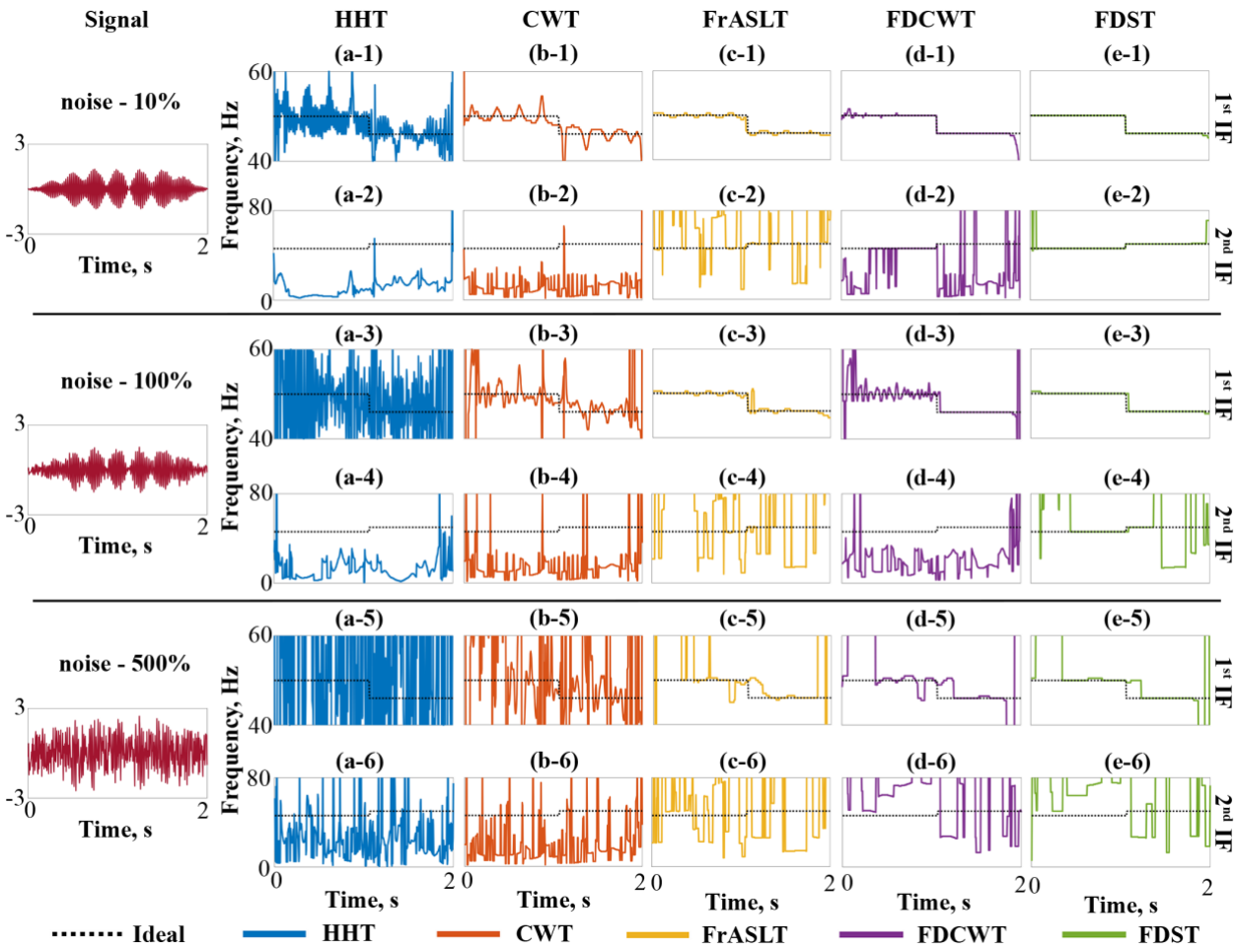

Fig. 7. The extracted both 1st and 2nd IF of the analytical signal with noise level of 10%, 100% and 500% using (a) HHT, (b) CWT, (c) FrASLT, (d) FDCWT and (e) FDST.

Table 2 provides the mean and standard deviation of the RMSE values of the IFs , across the 1000 instances (assessing the statistics for the added random error) of the analytical test signal set. Generally, HHT exhibited at least a 41% higher mean RMSE as compared to other methods. The 1st IF extracted by CWT exhibited a minimum of 71%, 6%, and 27% higher mean RMSE compared to FrASLT, FDCWT and FDST, respectively. The FDCWT demonstrated a mean RMSE improvement of 42% (10% noise), 5% (100% noise), and 23% (500% noise) compared to CWT. Both FrASLT and FDST in general exhibited highly accurate IF extraction owing to the super resolution of the FrASLT. Additionally, incorporating the Fourier-decomposition into FrASLT resulted in a 65% and 12% improvement for the 1st IF at 10% and 500% noise,

Table 2. The mean and standard deviation of RMSE (in Hz) of 1st and 2nd IF extraction with ground truth considering 1000 instances of test signal using HHT, CWT, FrASLT, FDCWT and FDST

Method / Noise %	HHT	CWT	FrASLT	FDCWT	FDST
1st IF					
10%	5.18 ± 0.77	2.31 ± 0.79	0.51 ± 0.02	1.35 ± 0.92	0.18 ± 0.06
100%	15.39 ± 1.24	9.52 ± 1.58	4.89 ± 3.49	9.00 ± 2.67	5.08 ± 3.45
500%	30.63 ± 1.49	21.67 ± 1.63	17.05 ± 4.34	16.79 ± 4.87	14.97 ± 5.60
2nd IF					
10%	38.02 ± 0.64	37.84 ± 0.90	35.13 ± 2.93	30.78 ± 1.48	6.91 ± 3.71
100%	35.96 ± 1.39	36.78 ± 0.94	39.11 ± 3.10	38.66 ± 4.47	29.53 ± 4.22
500%	32.33 ± 1.32	35.32 ± 1.03	38.43 ± 3.08	39.48 ± 5.63	38.95 ± 5.98

respectively, and a 4% decrease in performance at the 100% noise case. Similarly, the Fourier-decomposition step resulted in an RMSE improvement of 24-80% for the 2nd IF extraction at 10%-100% noise. However, even FDST failed to extract the 2nd IF with sufficient accuracy at 500% noise, due to the significant mixing of noise with signal dynamics. In general, this analysis emphasizes the superior performance of FDST at extracting the relevant dynamics, even in the presence of significant noise, and establishes that for noisy signals (i.e., >100% noise), only the primary dynamics (i.e., 1st IF) can be accurately extracted.

5. Pulsatile experimental PIV data analysis

5.1. Pulsatile experimental PIV data

5.1.1. Data collection and processing

Experimental transitional pulsatile pipe flow data was used to test the efficacy of our proposed method for evaluating intermittent flow structures and the instantaneous TKE spectrum. A sub-set

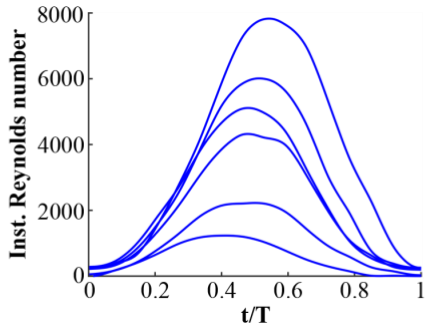

Fig. 8. The instantaneous Re for cases with mean Re of 500, 1000, 2000, 2500, 3000 and 4000

of the two-dimensional-two velocity component (2D-2C) planar PIV data from Brindise and Vlachos (2018) was used. We provide a brief description of the data here, but the reader should refer to Brindise and Vlachos (2018) for complete details on the experimental setup and captured data. Womersley number represents the ratio between inertial forces and viscous forces and is computed by:

$$\alpha = L\sqrt{\frac{\omega\rho}{\mu}} \tag{4}$$

where L is the characteristic length scale, ω is the angular frequency of pulsation, ρ is the density of the fluid, and μ is the dynamic viscosity of the fluid. For these experiments, a Wormsley number of 2.4 and tube diameter of 1/8'' was used. A symmetric (nearly sinusoidal) input pulsatile waveform shape was tested at six mean Reynolds numbers (Re) of 500, 1000, 2000, 2500, 3000 and 4000. Fig. 8, adapted from Brindise and Vlachos (2018), provides the Re versus time trend for each test case used here. The instantaneous Re ranged from zero to approximately twice the mean Re for all cases; this resulted in transitional and turbulent flow being present even for low mean Re cases.

All velocity fields and post-processed flow quantities used herein were those exactly computed in Brindise and Vlachos (2018), without modification. Briefly, velocity fields were collected using a double-pulsed (i.e., frame-straddling) image capture mode. The captured images were of size

2560×1600 pixels with a magnification of 2.29 μm/pixel. Image pairs were captured at 250 Hz with varied inter-frame times to ensure a maximum particle displacement of 15 pixels between frames. Resulting images were processed using three passes of an iterative image deformation algorithm (Scarano, 2001) with robust phase correlation (Eckstein and Vlachos, 2009a, 2009b; Eckstein et al., 2008) and a median-based universal outlier detection method (UOD) (Westerweel and Scarano, 2005) to compute the velocity fields. The extracted PIV velocity fields were post-processed using proper orthogonal decomposition (POD) (Sirovich, 1987) with the entropy line-fit (ELF) thresholding method (Brindise and Vlachos, 2017); the velocity fields were subsequently phase averaged. The mean velocity component was computed from the post-processed PIV velocity by reconstructing the 5th level approximate coefficient of the discrete wavelet transform (DWT). The axial and radial fluctuating velocities (u' and v', respectively) were calculated by subtracting the mean component from the post-processed PIV velocity. To compute turbulent kinetic energy (TKE), the axial average of u' was subtracted from u' and v' to minimize the effect of pump fluctuations (Trip et al., 2012).

5.1.2. *Post-processing calculations*

Since ground truth time-frequency information is not available for experimental data, rigorous error analysis across methods could not be performed. Instead, a pseudo-error analysis was performed by comparing a histogram of the spatiotemporal distribution (i.e., across all space and time) of the 1st dominant frequency of each TFR method (Fig. 9-1). The TFR histograms were compared to the FFT-computed, spatially-averaged power spectral density (PSD) of u' obtained by averaging the PSD for all spatial points. The FFT-based PSD was considered as the ground truth for the comparison. It is important to note that the FFT does not explicitly provide the temporal localization of frequencies resulting from non-stationary behaviors. However, the invertibility of the FFT implies that all frequency information is available within the FFT spectrum,

and dominant IFs (even non-stationary ones) are expected to manifest as major peaks in the FFT spectrum. The spatially-averaged FFT-based PSD and all spatiotemporal IF distributions were normalized based on their maximum values to ensure consistent comparison across methods. The peaks of the resulting normalized PSD and spatiotemporal IF distributions were then identified using the *findpeaks* function in MATLAB and sorted in descending order based on peak height. As the number of peaks obtained for the PSD and spatiotemporal distribution of each method is expected to differ, the lowest number of peaks out of all distributions were considered as the number of relevant peaks to ensure consistent comparison. Hence, relevant peaks of the PSD and spatiotemporal distribution of each method were identified, and the peak height was used as the measure of peak dominance. The frequencies corresponding to such peaks were extracted in the order of dominance for PSD and spatiotemporal distribution of each method. The RMSE between

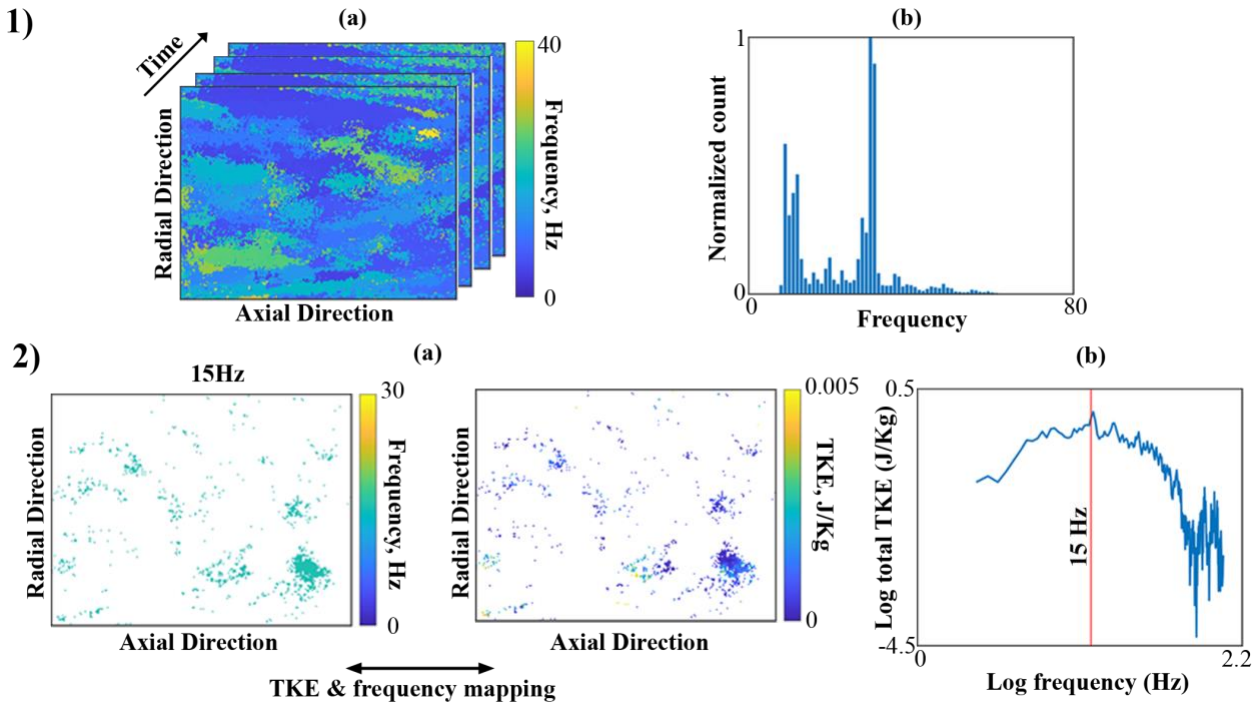

Fig. 9. The post-processing of IFs using (1) axial fluctuating velocity with pump fluctuations and (2) TKE. (1a) the spatial 1st IF stack across all time instant. (1b) calculation of spatiotemporal histogram by considering 1st IF corresponding to all time instant and spatial points. (2a) spatial mapping between spatial 1st IF and TKE snapshot for given frequency at a specific time instant. (2b) Calculation of instantaneous TKE spectrum by summing TKE at spatial points corresponding to each frequency.

the peak frequencies identified from the PSD and spatiotemporal distribution of each method was computed and considered as the error of each method.

To evaluate the relevant flow-based information contained within the IFs, the instantaneous TKE spectrum was computed using the 1st, 2nd, and 3rd IFs of the TKE. Fig. 9-2 illustratively describes the calculation of the instantaneous TKE spectrum for the 1st IF. For this calculation, the 2D spatial frequency maps of each IF and corresponding 2D TKE spatial maps at each time instant were considered. For each unique frequency, the TKE values for all spatial points which maintained that unique frequency were extracted (Fig 9-2a). These extracted TKE values were summed, resulting in the total TKE associated with the corresponding frequency at a given time instant (Fig 9-2b). This calculation was repeated for all frequencies, resulting in the instantaneous TKE spectrum at a particular time instant (Fig 9-2b). The instantaneous TKE spectrum was plotted on a logarithmic scale, and the trend was smoothed using a moving average filter with a window size of 10% of number of frequency scales used. The line corresponding to Kolmogorov scaling (slope of -5/3) was fitted to the smoothed instantaneous TKE spectrum. For each IF, the frequency range where the instantaneous TKE spectrum matched the Kolmogorov spectrum was identified. Coherent 2D spatial frequency structures as well as their area as a function of frequency were also evaluated. For this, a 2D median filter with window size of 3×3 pixels were used to smooth the spatial maps. Coherent frequency structures were identified using a standard connected component analysis. Spatial structure area was computed as the number of pixels in each identified connected component.

5.2. Pseudo-error analysis of TFR methods

The analytical signal analysis demonstrated that both FDCWT and FDST provided marked improvement in accurately extracting the IFs of ideal sinusoidal signals. Next, we compared the

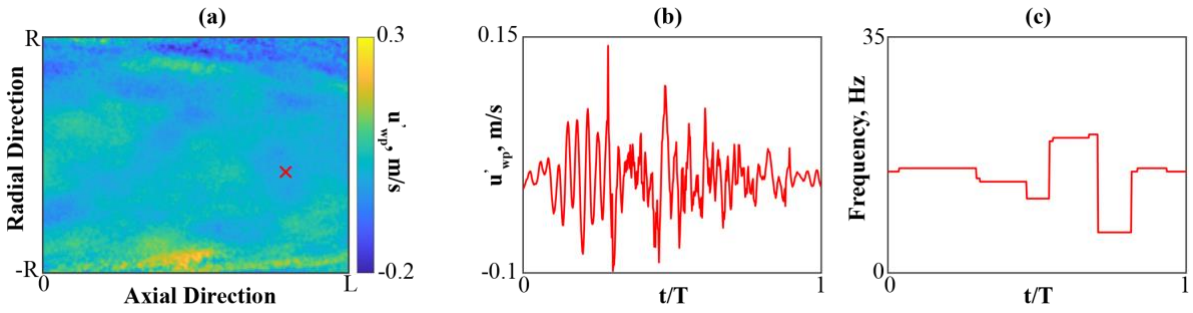

Fig. 10. The IF extraction using axial fluctuating velocity with pump fluctuations (u'_{wp}). (a) the snapshot of u'_{wp} at a given time instant. (b) temporal variation of u'_{wp} at specific spatial location. (c) The extracted 1st IF using FDST.

efficacy of the TFR methods using the experimental PIV data, which contains complex non-linear mechanisms and noise.

Fig. 10 illustrates the extraction of the 1st IF of u' for the spatial point denoted with a red 'X'. We selected u' as the input signal for this error analysis since the frequencies of the pump fluctuations are expected to precipitate stationary and non-stationary dynamics, which, in addition the flow dynamics, ensures the presence of secondary frequency mechanisms. Fig. 11a to 11e illustrate the representative distribution of the spatially-averaged PSD and spatiotemporal IFs for (a) HHT, (b) CWT, (c) FrASLT, (d) FDCWT, and (e) FDST, using the mean Re of 3000 test case. The spatially averaged PSD for this test case contained two dominant peaks at 4.5Hz and 15Hz along with additional minor peaks including ones at 6Hz and 10Hz. The RMSE comparing the spatially averaged PSD and the spatiotemporal IFs were 34.32Hz, 47.04Hz, 24.96Hz, 19.51Hz and 12.38Hz for HHT, CWT, FrASLT, FDCWT and FDST, respectively. The smoothness of the spatiotemporal IF trendlines for HHT and CWT (Fig. 11a and 11b) highlight that these methods smeared out physical dynamics of the flow. Practically, this demonstrates that HHT and CWT can only accurately identify 1-2 frequency components within a flow, making them ineffective for intermittency analysis. With FrASLT (Fig. 11c), this smearing occurred to a much lesser extent. However, FrASLT still failed to distinguish the minor peak at 6Hz from the dominant peak at 4.5Hz. Conversely, both of our proposed methods accurately identified the dominant frequency

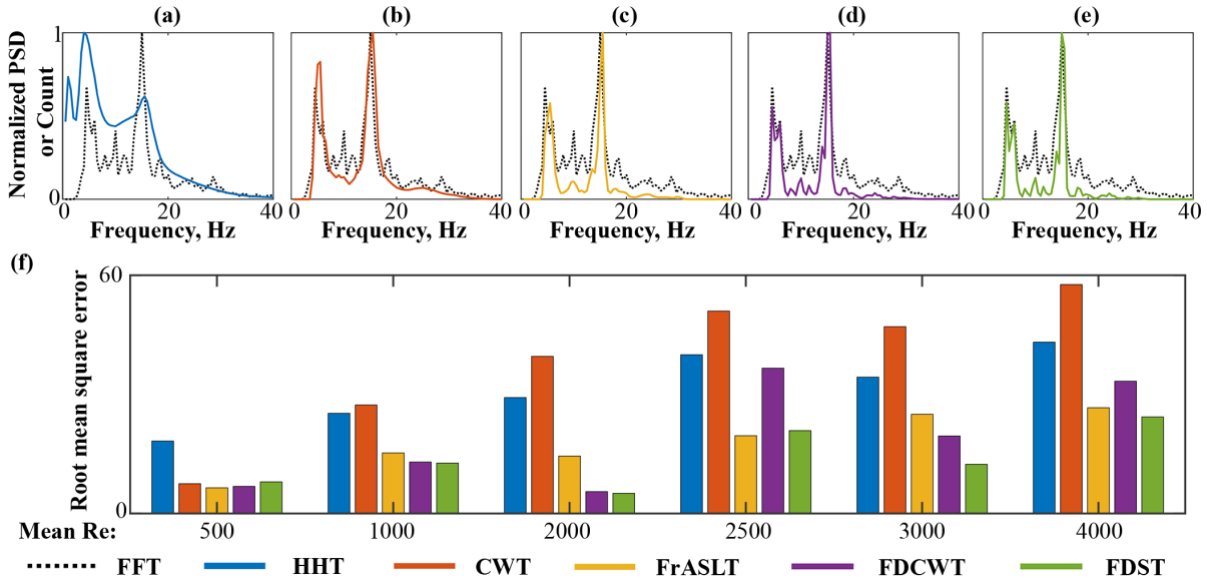

Fig. 11. Normalized spatial averaged PSD and the spatiotemporal 1st IF distribution for test case with mean Re of 3000 using (a) HHT (b) CWT (c) FrASLT (d) FDCWT and (e) FDST for axial fluctuation velocity with pump fluctuations. (f) RMSE between the frequencies correspond to the predominant peaks in both spatially averaged PSD and the spatiotemporal 1st IF distribution for all cases.

peaks as well as several (more than 7) tertiary peaks. This emphasizes that for flow analysis the Fourier mode decomposition step dramatically increases the accuracy and depth of the signal dynamics that can be extracted. Fig. 11f shows the RMSE for all experimental test cases. The average RMSE across all cases was 31.68Hz for HHT, 38.34Hz for CWT, 17.88Hz for FrASLT, 19.11Hz for FDCWT, and 13.88Hz for FDST. The adaptive Fourier windowing resulted in an average RMSE improvement of 50% for FDCWT over CWT and 22% for FDST over FrASLT. Moreover, FDST provided a 27% improvement of RMSE over FDCWT. This suggests that for extracting flow dynamics from real, noisy signals, a high frequency resolution is more important than the slight loss of temporal resolution.

5.3. Investigation of intermittency and scaling mechanism

Next, we evaluate the physical information and dynamics the IFs can describe within a flow. For this analysis, we only provide results using the FDST method since this was shown to provide the best performance for noisy signals and in Fig. 11. Fig. 12 shows the typical instantaneous energy cascade of the IFs in order to investigate the intermittency and resulting scaling mechanisms

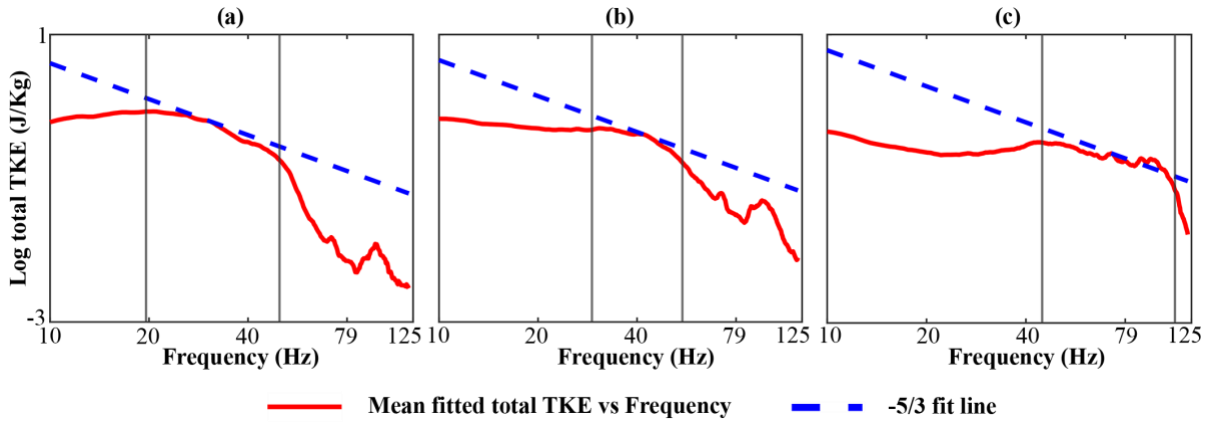

Fig. 12. Typical instantaneous TKE spectrum regarding (a) 1st, (b) 2nd and (c) 3rd IFs.

present in pulsatile flows. For Fig. 12, a representative instantaneous TKE spectrum computed using the (a) 1st, (b) 2nd, and (c) 3rd IFs of the 4000 mean Re test case. For the time step shown, the instantaneous Re is approximately 7500. The dashed blue line represents the -5/3 Kolmogorov scaling and the window denoted by the two black vertical lines denote the frequency range where the instantaneous TKE spectrum follows the Kolmogorov scaling to within a TKE tolerance of 0.2 in log scale. In general, the instantaneous TKE spectrum corresponding to the 1st, 2nd, and 3rd IFs was found to exhibit similar behavior to the traditionally obtained Kolmogorov energy spectrum. Specifically, a power-law behavior (linear behavior in logarithmic scale) was observed in certain regions of the instantaneous TKE spectrum, implying a scale free nature of the energy transfer at these frequencies. However, unlike the traditional energy spectrum, which is stationary in nature, the instantaneous TKE spectrum represents flow behavior at a particular time instant. Thus, the instantaneous TKE spectrum is particularly beneficial for studying dissipation mechanisms in non-uniform flows such as pulsatile flows where flow dynamics are not constant in time. The Fig. 12 reiterates these notions. In Fig. 12, the instantaneous TKE spectrum matched the Kolmogorov scaling for the frequency ranges of 19.5 to 49.6Hz for the 1st IF, 29.1 to 54.6Hz for the 2nd IF, and 44.6 to 112.2Hz for the 3rd IF. This suggests that each IF component extracted using our proposed method describes partially independent scaling mechanisms inherent in the pulsatile flows.

Moreover, because the windows of each IF cascade to larger frequencies (i.e., the 1st IF had a lower frequency window than the 2nd, etc.), it is expected that the IFs decompose and, to an extent, reveal the cascade of turbulent structures in the flow. Given that the turbulent cascade represents the breakdown of turbulent structures into increasingly smaller eddies, this notion implies that the first IF should describe the largest structures, while the 3rd describes the smallest structures (of the three IFs analyzed). Moreover, because the IFs are evaluated at each spatiotemporal point in the flow field, it advantageously enables frequency structures to be evaluated from a spatiotemporal perspective.

Fig. 13a, 13b, and 13c show the spatial frequency distribution of each IF, limited to only the frequencies within the Kolmogorov spectrum matching window (all other frequencies are shown in white). Spatial maps for the three mean Re cases at the max TKE time instant are shown. Fig.

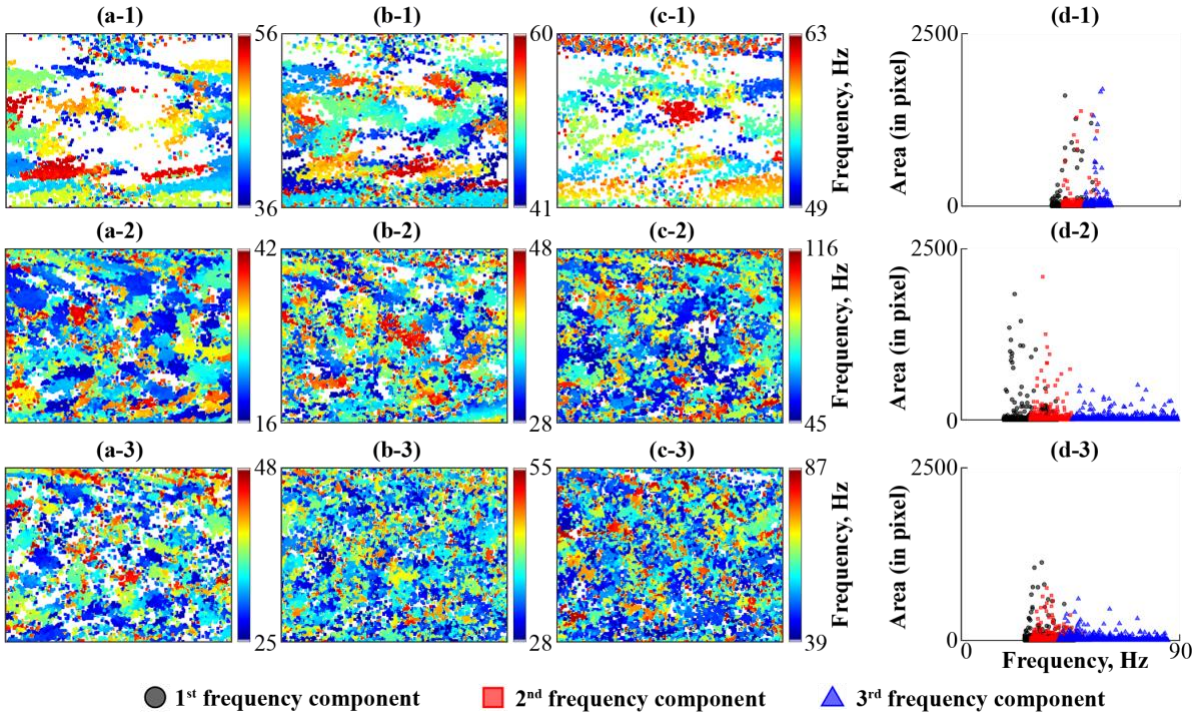

Fig. 13. The spatial distribution of IFs associated with energy cascade regarding a) 1st, (b) 2nd and (c) 3rd IF components and (d) area of each spatial structures for test cases with mean Re of (1) 1000 (2) 2500 and (3) 4000.

13d shows the area of each individual structure vs. the mean frequency of the structure. The area of the spatial IF structures generally decreased in size with increasing mean Re as well as increasing IF level. At the low mean Re's of 1000 (Fig. 13a), the structures were primarily large, axially oriented patterns. As the mean Re increased, finer and finer frequency structures began to emerge for all IF components. At high mean Re's, the 1st IF spatial structures retained some axial orientation, especially at the near wall regions. Prior studies have noted theoretical predictions of the presence of these types of structures in pulsatile flows as a consequence of helical and axisymmetric disturbances (Xu et al., 2021). However, for the 2nd and 3rd IFs, no axial pattern of the spatial frequency structures was discernible. This suggests that the IF spatial structures, at least in part, describe the dissipation of axial structures within transition to turbulence in pulsatile flows. Fig. 13d illustrates that for the transitional and turbulent mean Re cases (Fig. 13d-2 and 13d-3), the area of the structures decreased roughly exponentially with increasing frequency components.

Table 3 quantitatively explores this, providing the average area of the spatial frequency structures associated with each IF. The mean area of the spatial frequency structures across all three IFs were 58 pixels, 28 pixels, 18 pixels, 17 pixels, 14 pixels, and 13 pixels for test cases with mean Re's of 500, 1000, 2000, 2500, 3000, and 4000, respectively. This confirms the rapid decline and then plateau of structure size as the Re increases from the laminar to transitional and turbulent

Table 3. Mean area (in pixels) of all spatial frequency structures as a function of IF (1st, 2nd, and 3rd) and mean Re of the test case

Mean Re / Frequencies	500	1000	2000	2500	3000	4000
1st inst. frequency	74	30	27	24	18	18
2nd inst. frequency	54	24	14	18	14	13
3rd inst. frequency	45	31	11	10	10	9

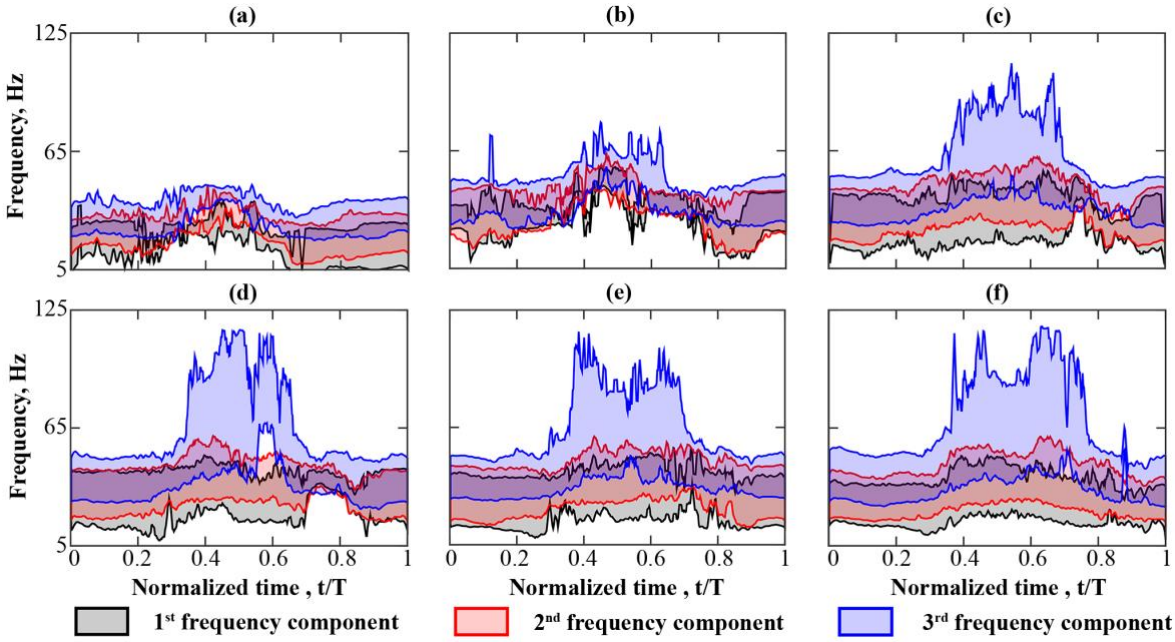

Fig. 14. Temporal variation of instantaneous energy cascade scales of all test cases with symmetric waveforms and mean Re of (a) 500 (b) 1000 (c) 2000 (d) 2500 (e) 3000 and (f) 4000.

regimes. Overall, this further suggests that the spatial frequency structures reveal turbulent structures across the Kolmogorov scale.

Fig. 14 illustrates the temporal variation of the energy cascade scaling range window for all mean Re test cases (where the max flowrate occurs at t/T of about 0.5), considering all spatial points. Specifically, the lower and upper bound of the black, red, and blue shaded regions represent the starting and ending frequency of the energy cascade scaling window for the 1st, 2nd, and 3rd IF components, respectively. At the low mean Re's of 500 and 1000, the energy cascade of all three dominant frequency components behaved similarly with scaling ranges between 5 and 65Hz for nearly all-time instants. Interestingly, the energy cascade windows of the 1st and 2nd IFs remained largely the same across all mean Re cases. This suggests that these IFs primarily represent instabilities and unsteadiness associated with the pulsatile flow. Conversely, the energy cascade window of the 3rd IF differed significantly across mean Re cases. For the mean Re cases from 2000-4000 (Fig. 14c-14f), the upper frequency bound of the energy cascade window increased rapidly and plateaued for a length of time before decreasing rapidly. Specifically, for the mean Re

2000 case, the upper bound of the 3rd IF increased from t/T of 0.35 to 0.70, with an average frequency of 84Hz. Meanwhile, for the 2500, 3000, and 4000 mean Re cases, this upper bound increased from t/T of 0.30 to 0.71 (avg. freq. of 89Hz), 0.27 to 0.78 (avg. freq. of 79Hz), and 0.28 to 0.77 (avg. freq. of 88Hz), respectively. This suggests that the 3rd IF primarily describes structures associated with transition and turbulence and can provide valuable physical details of the flow. For example, the involvement of finer scales implies the dominance of viscous dissipation at higher instantaneous Re. Additionally, Fig.14 demonstrates that the scaling range windows of the instantaneous energy cascade may be able to inform a flow's progression of transition and turbulence in pulsatile flows. Specifically, by identifying the length and frequency of the plateau in the temporal variation of the energy cascade window range, transition from laminar to turbulent regimes in pulsatile flow may be able to be more precisely pinpointed. This notion, as well as its universality, should be explored in future work. Overall, this analysis highlights that our proposed FDST method is able to accurately decompose the flow into energy cascade structures and provide insight on the development of transitional and turbulent flow regimes.

6. Limitations

Several limitations of our method and this study exist. Since our method utilized CWT and FrASLT as the wavelet-based transforms to obtain the TFR modes, shortcomings of both CWT and FrASLT, such as the high computation cost of FrASLT, similarly impact our method. Furthermore, frequency and time resolution of FrASLT depends on the number of cycles and order of the superlet. Thus, the result obtained from the proposed FDST method heavily depends on the choice of these parameters. Our analysis suggested our choice of these parameters was optimal for this application, but alternative settings may be preferred for other applications. Since FrASLT

uses a combination of CWTs, inverting the superlet transform to obtain the original signal is difficult, as the amplitude and phase information from each CWT calculation gets lost in combination. Thus, the FDST is not invertible. Furthermore, the Fourier-based decomposition was based on the major peaks in the Fourier spectrum. Hence, our method heavily depends upon the accurate detection and separation of relevant and noisy peaks from the Fourier spectrum. Additionally, we restricted the TFR of the Fourier decomposition modes to the corresponding frequency band as shown in Fig. 2d and 2e, possibly resulting in loss of some information due to the removal of the energy content outside the frequency band. The experimental data used for this study was collected with planar PIV such that three-dimensional dynamics could not be resolved. Additionally, the axial field of view of the pipe was not large enough to resolve turbulent puffs, such that the IFs of these transitional structures could not be explored. The ability of our method to decompose spatial scales of the turbulent energy cascade would be limited by the resolution of the flow data being evaluated, a notion which should be explored in future work. Furthermore, because we tested the method using only pulsatile data, the pulsatile mechanisms described by the IFs could not be concretely and explicitly resolved. Future work should aim to apply our method to steady and pulsatile flows to explore this.

7. Conclusion

In this work, we present a novel TF method, the Fourier-decomposed wavelet-based transform, to evaluate intermittency in transitional and turbulent flows. The proposed method aims to enhance the TFR of a signal by addressing the interference artifacts arising from low resolution in TFR. This is achieved by decomposing the signal of interest into a set of Fourier modes and combining the TFR of each mode function into a single accurate TFR. Using analytical test signals, we

demonstrated that our method accurately extracted the primary and secondary instantaneous dynamics of the underlying system, and yielded improved results as compared to current TF methods. Furthermore, our investigation using a pulsatile, transitional experimental PIV dataset revealed that each IF component, as extracted by FDST, decomposed the Kolmogorov energy cascade inherent in the flow. Moreover, we demonstrated that analyzing the spatial frequencies associated with IFs can provide valuable insights into the scaling mechanisms and the progression of turbulence in pulsatile flows. Overall, the result of this study demonstrated the importance of addressing the interference artifacts in TFR calculations, and underscored the advantage of investigating spatial IF structures for understanding the mechanisms related to transition and turbulence flows. Future work should focus on comparing such IF structures to other commonly computed ones such as coherent structures, as well as compare our method to other spectral and decomposition methods such as POD, spectral POD (sPOD), and dynamic mode decomposition (DMD).

Funding: This work was supported by a National Science Foundation (NSF) grant (Award number 2335760).

Author contributions: JJK contributed to formal analysis; investigation; methodology; writing - original draft. NS contributed to investigation; methodology. MB contributed to conceptualization; investigation; project administration; supervision; writing - review and editing.

Data availability: The data that support the findings of this study are available from the corresponding author upon reasonable request.

DECLARATIONS

Conflict of Interest: The authors have no conflicts to disclose.

REFERENCES

Addison, P.S., 2017. The illustrated wavelet transform handbook: introductory theory and applications in science, engineering, medicine and finance, Second edition. ed. CRC Press, Taylor & Francis Group, Boca Raton, FL.

Avila, K., Moxey, D., de Lozar, A., Avila, M., Barkley, D., Hof, B., 2011. The Onset of Turbulence in Pipe Flow. Science 333, 192–196. https://doi.org/10.1126/science.1203223

Barzan, H., Moca, V.V., Ichim, A.-M., Muresan, R.C., 2021. Fractional Superlets, in: 2020 28th European Signal Processing Conference (EUSIPCO). Presented at the 2020 28th European Signal Processing Conference (EUSIPCO), IEEE, Amsterdam, Netherlands, pp. 2220–2224. https://doi.org/10.23919/Eusipco47968.2020.9287873

Brindise, M.C., Vlachos, P.P., 2018. Pulsatile pipe flow transition: Flow waveform effects. Physics of Fluids 30, 015111. https://doi.org/10.1063/1.5021472

Brindise, M.C., Vlachos, P.P., 2017. Proper orthogonal decomposition truncation method for data denoising and order reduction. Exp Fluids 58, 28. https://doi.org/10.1007/s00348-017-2320-3

Eckstein, A., Vlachos, P.P., 2009a. Digital particle image velocimetry (DPIV) robust phase correlation. Meas. Sci. Technol. 20, 055401. https://doi.org/10.1088/0957-0233/20/5/055401

Eckstein, A., Vlachos, P.P., 2009b. Assessment of advanced windowing techniques for digital particle image velocimetry (DPIV). Meas. Sci. Technol. 20, 075402. https://doi.org/10.1088/0957-0233/20/7/075402

Eckstein, A.C., Charonko, J., Vlachos, P., 2008. Phase correlation processing for DPIV measurements. Exp Fluids 45, 485–500. https://doi.org/10.1007/s00348-008-0492-6

Einav, S., Sokolov, M., 1993. An Experimental Study of Pulsatile Pipe Flow in the Transition Range. Journal of Biomechanical Engineering 115, 404–411. https://doi.org/10.1115/1.2895504

Farge, M., 1992. Wavelet Transforms and Their Applications to Turbulence. Annual Review of Fluid Mechanics 24, 395–458. https://doi.org/10.1146/annurev.fl.24.010192.002143

Freidoonimehr, N., Arjomandi, M., Sedaghatizadeh, N., Chin, R., Zander, A., 2020. Transitional turbulent flow in a stenosed coronary artery with a physiological pulsatile flow. International Journal for Numerical Methods in Biomedical Engineering 36, e3347. https://doi.org/10.1002/cnm.3347

Frishman, A., Grafke, T., 2022. Dynamical landscape of transitional pipe flow. Phys. Rev. E 105, 045108. https://doi.org/10.1103/PhysRevE.105.045108

Huang, N.E., Shen, Z., Long, S.R., Wu, M.C., Shih, H.H., Zheng, Q., Yen, N.-C., Tung, C.C., Liu, H.H., 1998. The empirical mode decomposition and the Hilbert spectrum for nonlinear and non-stationary time series analysis. Proceedings of the Royal Society of London. Series A: Mathematical, Physical and Engineering Sciences 454, 903–995. https://doi.org/10.1098/rspa.1998.0193

Huang, Y.X., Schmitt, F.G., Lu, Z.M., Liu, Y.L., 2008. An amplitude-frequency study of turbulent scaling intermittency using Empirical Mode Decomposition and Hilbert Spectral Analysis. EPL 84, 40010. https://doi.org/10.1209/0295-5075/84/40010

Kefayati, S., Poepping, T.L., 2013. Transitional flow analysis in the carotid artery bifurcation by proper orthogonal decomposition and particle image velocimetry. Medical Engineering & Physics 35, 898–909. https://doi.org/10.1016/j.medengphy.2012.08.020

Lilly, J.M., 2017. Element analysis: a wavelet-based method for analysing time-localized events in noisy time series. Proc. R. Soc. A. 473, 20160776. https://doi.org/10.1098/rspa.2016.0776

Moca, V.V., Bârzan, H., Nagy-Dăbâcan, A., Mureşan, R.C., 2021. Time-frequency super-resolution with superlets. Nat Commun 12, 337. https://doi.org/10.1038/s41467-020-20539-9

Nerem, R.M., Seed, W.A., Wood, N.B., 1972. An experimental study of the velocity distribution and transition to turbulence in the aorta. Journal of Fluid Mechanics 52, 137–160. https://doi.org/10.1017/S0022112072003003

Peacock, J., Jones, T., Tock, C., Lutz, R., 1998. The onset of turbulence in physiological pulsatile flow in a straight tube. Experiments in Fluids 24, 1–9. https://doi.org/10.1007/s003480050144

Poelma, C., Watton, P.N., Ventikos, Y., 2015. Transitional flow in aneurysms and the computation of haemodynamic parameters. Journal of The Royal Society Interface 12, 20141394. https://doi.org/10.1098/rsif.2014.1394

Ruppert-Felsot, J., Farge, M., Petitjeans, P., 2009. Wavelet tools to study intermittency: application to vortex bursting. Journal of Fluid Mechanics 636, 427–453. https://doi.org/10.1017/S0022112009008003

Scarano, F., 2001. Iterative image deformation methods in PIV. Meas. Sci. Technol. 13, R1. https://doi.org/10.1088/0957-0233/13/1/201

Sherwin, S.J., Blackburn, H.M., 2005. Three-dimensional instabilities and transition of steady and pulsatile axisymmetric stenotic flows. Journal of Fluid Mechanics 533, 297–327. https://doi.org/10.1017/S0022112005004271

Singh, P., Joshi, S.D., Patney, R.K., Saha, K., 2017. The Fourier decomposition method for nonlinear and non-stationary time series analysis. Proc. R. Soc. A. 473, 20160871. https://doi.org/10.1098/rspa.2016.0871

Sirovich, L., 1987. Turbulence and the dynamics of coherent structures. I. Coherent structures. Quart. Appl. Math. 45, 561–571. https://doi.org/10.1090/qam/910462

Trip, R., Kuik, D.J., Westerweel, J., Poelma, C., 2012. An experimental study of transitional pulsatile pipe flow. Phys. Fluids 24, 014103. https://doi.org/10.1063/1.3673611

Valen-Sendstad, K., Mardal, K.-A., Mortensen, M., Reif, B.A.P., Langtangen, H.P., 2011. Direct numerical simulation of transitional flow in a patient-specific intracranial aneurysm. Journal of Biomechanics 44, 2826–2832. https://doi.org/10.1016/j.jbiomech.2011.08.015

Westerweel, J., Scarano, F., 2005. Universal outlier detection for PIV data. Exp Fluids 39, 1096–1100. https://doi.org/10.1007/s00348-005-0016-6

Xu, D., Song, B., Avila, M., 2021. Non-modal transient growth of disturbances in pulsatile and oscillatory pipe flows. J. Fluid Mech. 907, R5. https://doi.org/10.1017/jfm.2020.940

Yochum, M., Renaud, C., Jacquir, S., 2016. Automatic detection of P, QRS and T patterns in 12 leads ECG signal based on CWT. Biomedical Signal Processing and Control 25, 46–52. https://doi.org/10.1016/j.bspc.2015.10.011

Yuan, H., Tan, S., Zhuang, N., Lan, S., 2016. Flow and heat transfer in laminar–turbulent transitional flow regime under rolling motion. Annals of Nuclear Energy 87, 527–536. https://doi.org/10.1016/j.anucene.2015.10.009

Zhou, W., Feng, Z., Xu, Y.F., Wang, X., Lv, H., 2022. Empirical Fourier decomposition: An accurate signal decomposition method for nonlinear and non-stationary time series

analysis. Mechanical Systems and Signal Processing 163, 108155. https://doi.org/10.1016/j.ymssp.2021.108155

Zhuang, N., Tan, S., Yuan, H., 2016. The friction characteristics of low-frequency transitional pulsatile flows in narrow channel. Experimental Thermal and Fluid Science 76, 352–364. https://doi.org/10.1016/j.expthermflusci.2016.03.030